

# Bias Impact Analysis and Calibration of Terrestrial Mobile LiDAR System With Several Spinning Multibeam Laser Scanners

Radhika Ravi<sup>ID</sup>, Yun-Jou Lin, Magdy Elbahna, Tamer Shamseldin, and Ayman Habib

**Abstract**—This paper proposes a multiunit light detection and ranging (LiDAR) system calibration procedure to directly estimate the mounting parameters relating multiple spinning multibeam laser scanners to the global navigation satellite system/inertial navigation system (GNSS/INS) unit onboard a mobile terrestrial platform in order to derive point clouds with high-positional accuracy. This procedure is based on the use of conjugate planar/linear features in overlapping point clouds derived from different drive runs. In order to increase the efficiency of semiautomatic conjugate feature extraction from LiDAR data, specifically designed calibration boards covered by highly reflective surfaces that could be easily deployed and set up within outdoor environments are used in this paper. To ensure the accuracy of the estimated mounting parameters, an optimal configuration of target primitives and drive runs is determined by analyzing the potential impact of bias in mounting parameters of a LiDAR unit on the resultant point cloud for different orientations of target primitives and different drive run scenarios. This impact is also verified experimentally by simulating a bias in each mounting parameter separately. Finally, the optimal configuration is used within an experimental setup to evaluate the performance of the proposed calibration procedure through the *a posteriori* variance factor of least squares adjustment and the quality of fit of adjusted point cloud to linear/planar surfaces before and after the calibration process. The proposed calibration approach attained an accuracy of 1.42 cm, which is better than the accuracy expected based on the specifications of the involved hardware components, i.e., the LiDAR and GNSS/INS units.

**Index Terms**—Bias impact analysis, calibration, least squares adjustment (LSA), light detection and ranging (LiDAR) system.

## I. INTRODUCTION

LASER scanners onboard airborne and terrestrial platforms have been established as a proven technology for the acquisition of dense point clouds with high-positional accuracy. The main factors behind the widespread use of light detection and ranging (LiDAR) systems include the ever-continuous improvement in global navigation satellite system/inertial navigation system (GNSS/INS) direct georeferencing technology as well as enhanced performance and

Manuscript received August 28, 2017; revised November 18, 2017 and January 5, 2018; accepted February 28, 2018. Date of publication March 21, 2018; date of current version August 27, 2018. This work was supported in part by the Joint Transportation Research Program, Indiana Department of Transportation and Purdue University, and in part by the Advanced Research Projects Agency-Energy, U.S. Department of Energy, under Award DE-AR0000593. (Corresponding author: Ayman Habib.)

The authors are with the Lyles School of Civil Engineering, Purdue University, West Lafayette, IN 47907-1971 USA (e-mail: ravi22@purdue.edu; lin599@purdue.edu; melbahn@purdue.edu; tshamsel@purdue.edu; ahabib@purdue.edu).

Color versions of one or more of the figures in this paper are available online at <http://ieeexplore.ieee.org>.

Digital Object Identifier 10.1109/TGRS.2018.2812782

reduced size and cost of laser scanning units. Currently, there are commercially available LiDAR units that are capable of emitting more than a quarter million pulses per second at a cost of less than U.S. \$10k. Such availability, together with the ever-increasing range of applications—such as digital building model generation, transportation corridor monitoring, telecommunications, precision agriculture, infrastructure monitoring, seamless outdoor–indoor mapping, and power line clearance evaluation [1]–[4]—have led to the development of multiunit mobile LiDAR systems onboard airborne and terrestrial platforms that are either manned or unmanned. However, the attainment of the full positioning potential of such systems is contingent on an accurate calibration of the mobile mapping unit as a whole. Habib *et al.* [5] studied the impact of airborne LiDAR system calibration on the relative and absolute accuracy of the derived point clouds, both qualitatively and quantitatively. The relative accuracy was evaluated by quantifying the degree of coalignment of overlapping strips before and after calibration, whereas the absolute accuracy was evaluated by quantifying the degree of compatibility between LiDAR and control surfaces before and after calibration. This paper proposes a multiunit LiDAR system calibration strategy to directly estimate the mounting parameters relating spinning multibeam laser scanners to the GNSS/INS unit onboard a mobile mapping platform.

The cost-effective Velodyne laser scanner, which is a spinning multibeam laser unit and can rapidly capture a high volume of data, has been used in many mobile mapping systems and robotics applications [6]–[8]. Over the past few years, a great deal of research has been devoted to modeling the inherent systematic errors in Velodyne laser scanners as well as the calibration of LiDAR systems [9], [10]. Underwood *et al.* [11] calibrated the extrinsic parameters relating a SICK LMS-291 to a NovAtel synchronized position attitude navigation (SPAN) system by minimizing the discrepancy between sensed data and a known structure (i.e., a vertical pole and relatively flat ground). Muhammad and Lacroix [12] performed calibration of a rotating multibeam LiDAR with the objective to align the scan data as close as possible to a ground truth environment. He *et al.* [13] used pairwise multitype 3-D geometric features (i.e., point, line, and plane) to derive the extrinsic parameters between 2-D LiDAR and global positioning system (GPS)/inertial measurement unit (IMU). First, the points are segmented into different features and their quality is evaluated to compute weights to be used in the minimization of normal distance between

conjugate features. However, when the initial parameters are considerably inaccurate, the segments and derived weights may not be reliable. Chan *et al.* [14] introduced an intrinsic parameters calibration using vertical cylindrical features for Velodyne HDL-32E based on static stations and also analyzed the temporal stability of range measurements which indicated an approximate warm-up time of 2000 s for most laser beams. Glennie *et al.* [15] performed a geometric calibration using planar features scanned by stationary VLP-16 to marginally improve the accuracy of the point clouds by approximately 20%. Moreover, they also investigated the range accuracy of VLP-16, which is quoted to have an root mean square error (RMSE) value between 22 to 27 mm in the factory supplied calibration certificate. It was observed that some of the laser beams have worse range accuracy than the others.

The above discussion indicates that although many LiDAR system calibration procedures have been developed in the past, outdoor calibration of integrated GNSS/INS and multiunit 3-D laser scanners is still an active area of research. This paper focuses on a potential calibration technique for a LiDAR system with several spinning multibeam laser scanners onboard a terrestrial mobile mapping vehicle. The focus of the system calibration is to simultaneously estimate the mounting parameters relating the different system components by minimizing the discrepancy between conjugate linear and/or planar features in overlapping point clouds derived from different drive runs. More specifically, the lever arm and boresight angles relating the individual laser scanners and the onboard GNSS/INS unit are derived using an iterative calibration procedure. The proposed approach helps in overcoming several limitations of previously developed LiDAR system calibration procedures. First, the calibration procedures suggested by Chan *et al.* [14] and Glennie *et al.* [15] only estimate the intrinsic parameters of a single laser scanner and deal with point clouds captured from stationary scanners. On the contrary, the calibration approach proposed in this paper deals with mobile mapping systems and is capable of estimating the mounting parameters of multiple laser scanners simultaneously, thus facilitating an accurate alignment between point clouds captured by different sensors. Moreover, this paper deals with directly georeferenced point clouds, which would also ensure the alignment between point clouds captured from different survey missions. While Chan *et al.* [14] use only vertical cylindrical features and Glennie *et al.* [15] use only planar features for calibration, the approach proposed in this paper incorporates both linear and planar features found in outdoor environments to generate more accurate calibration results. Furthermore, unlike the calibration strategy proposed by Muhammad and Lacroix [12], in this paper, we eliminate the need for ground truth by proposing a calibration approach that aims at minimizing the discrepancy between geometric tie features (lines and planes) scanned in different drive runs. Another point of emphasis is that the proposed approach deals with a model considering a reference sensor and slave sensors, which provides the flexibility to conduct an indoor calibration of the mobile mapping system to derive the mounting parameters relating the slave sensors to the reference sensors, followed by an outdoor calibration to estimate the

mounting parameters relating the reference scanner to the onboard GNSS/INS unit, which in turn would relate all the laser scanners to the GNSS/INS unit.

Before proceeding with the calibration strategy, first an optimal configuration of target primitives setup and drive runs needs to be determined to maximize the impact of the systematic errors in question which would lead to a more accurate calibration. So, an analysis needs to be conducted to deduce the impact of bias in each of the mounting parameters of a LiDAR unit on the resultant point cloud. Habib *et al.* [16] discussed the bias impact analysis in detail for airborne linear scanners while describing the simplified and quasi-rigorous approaches for calibration, whereas in this paper, the bias impact analysis is conducted for a spinning multibeam laser scanner starting from the 3-D point positioning equation. The optimal configuration of target primitives for calibration can then be established by studying the impact of biases on planes oriented in different directions. Similarly, the optimal drive-run configuration is determined according to the effect of biases on the planes corresponding to drive runs in different directions and with varying separation. The conclusions drawn based on the results are then validated by simulating a bias in each of the mounting parameters one by one and studying the difference between the resultant and original point clouds. These results are quantified in terms of the RMSE of normal distances between the derived point clouds and best-fitting plane for various planar features oriented in different directions for different drive run configurations.

For the experimental evaluation of the performance of the proposed multiunit mobile LiDAR system calibration procedure, this paper uses a system consisting of a Velodyne HDL-32E laser scanner, a Velodyne VLP-16 laser scanner, and a SPAN-CPT direct georeferencing GNSS/INS unit. The performance of the calibration procedure is evaluated through the *a posteriori* variance factor of the least squares adjustment (LSA) procedure and the quality of fit of the adjusted point clouds to planar surfaces before and after the calibration process.

## II. THEORETICAL BIAS IMPACT ANALYSIS

### A. Conceptual Basis of a Multiunit LiDAR Point Positioning

A typical LiDAR system consisting of spinning multi-beam laser scanners could involve three coordinate systems (i.e., mapping frame, IMU body frame, and laser unit frame). A given point,  $I$ , acquired from a mobile mapping system can be reconstructed in the mapping coordinate system using (1), which is graphically illustrated in Fig. 1. The vector and matrix notations used in this paper are as follows.

- 1)  $r_a^b$  denotes the coordinates of point “ $a$ ” relative to point “ $b$ ” in the coordinate system associated with point “ $b$ .“
- 2)  $R_a^b$  denotes the rotation matrix that transforms a vector defined relative to the coordinate system “ $a$ ” into a vector defined relative to the coordinate system “ $b$ .“

For the laser unit frame, the origin is defined at the laser beams firing point and the  $Z$ -axis is along the axis of rotation of the laser unit. For a Velodyne system, each laser beam is fired at a fixed vertical angle,  $\beta$ ; the horizontal angle  $\alpha$  is

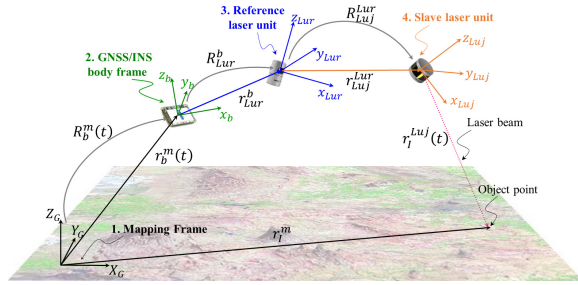


Fig. 1. Illustration of point positioning of a multiunit LiDAR system.

determined based on the rotation of the unit; and the range  $\rho$  is defined by the distance between firing point and its footprint. So, the coordinates of a 3-D point relative to the laser unit coordinate system,  $r_I^{luj}(t)$ , is defined by (2). For a multiunit LiDAR system, one of the laser scanners is set as reference and the rest are considered to be slave sensors. The reference sensor (lur) is related to the IMU body frame by a rigidly defined lever arm,  $r_{lur}^b$ , and boresight matrix,  $R_{lur}^b$ . Similarly, each slave sensor (luj) is related to the reference one (lur) by a rigidly defined lever arm,  $r_{luj}^b$ , and boresight matrix,  $R_{luj}^{lur}$ . The GNSS/INS integration provides the time-dependent position,  $r_b^m(t)$ , and rotation,  $R_b^m(t)$ , relating the mapping frame and IMU body frame coordinate systems, according to the optimized solution from the available GNSS and inertial measurements. One should note that such a LiDAR system can also be modeled by directly relating each of the laser scanners to the IMU body frame but the current model is preferred due to the fact that it allows for the derivation of the mounting parameters relating the slave sensors to the reference one without the need for GNSS/INS position and orientation information

$$\begin{aligned} r_I^m &= r_b^m(t) + R_b^m(t) r_{lur}^b + R_b^m(t) R_{lur}^b r_{luj}^{lur} \\ &\quad + R_b^m(t) R_{lur}^b R_{luj}^{lur} r_I^{luj}(t) \end{aligned} \quad (1)$$

$$r_I^{luj}(t) = \begin{pmatrix} x \\ y \\ z \end{pmatrix} = \begin{pmatrix} \rho(t) \cos \beta(t) \cos \alpha(t) \\ \rho(t) \cos \beta(t) \sin \alpha(t) \\ \rho(t) \sin \beta(t) \end{pmatrix}. \quad (2)$$

### B. Theoretical Bias Impact Analysis for Spinning Multibeam Laser Scanners

The objective of bias impact analysis is to derive a mathematical formulation that shows the deformations/shifts of points along planar patches (with different orientations and scanned from different drive runs) due to the presence of bias in the system mounting parameters. This analysis is carried out for a single unit LiDAR system, which implies that all the points are acquired by the reference laser unit. So, in (1),  $r_{luj}^{lur}$  would be zero and  $R_{luj}^{lur}$  would be an identity matrix, thus leading to (3), where the single laser unit is denoted by lu. It is to be noted that this analysis would also be valid for multiunit LiDAR systems as the latter can be considered as an integration of several single unit LiDAR systems together

$$r_I^m = r_b^m(t) + R_b^m(t) r_{lu}^b + R_b^m(t) R_{lu}^b r_I^{lu}(t). \quad (3)$$

Planar features are specifically used for conducting this analysis because they facilitate the observation of positional

deformations in one direction at a time, i.e., the effect in the direction normal to the plane. Ideally, the IMU is assumed to be perfectly vertical, i.e., the Z-axis of the IMU body frame is assumed to be perfectly aligned with the vertical direction of the mapping frame. However, this assumption might not always hold. So, in this paper, the bias impact analysis is carried out for a nearly vertical system, i.e., the potential tilt of the IMU body frame is incorporated in the analysis. The mathematical impact is verified through a numerical analysis of LiDAR data captured by a spinning multibeam laser scanner (for instance, Velodyne HDL-32E)

### C. Bias Impact Analysis: Nearly Vertical System

For mobile systems, the IMU is usually set up on the vehicle such that its X-, Y-, and Z-axes are aligned along the starboard, drive run, and vertical directions, respectively. In other words, the IMU body frame is parallel to the vehicle coordinate system. In order to generalize the bias impact analysis regardless of the orientation of the LiDAR unit relative to the IMU/vehicle coordinate system, the LiDAR point positioning equation is slightly modified by introducing a virtual LiDAR unit frame, Lu', which is almost aligned with the IMU body frame (or, the vehicle coordinate system). This facilitates the decision as to whether the impact is along/across the drive run and vertical directions. Moreover, the use of a virtual LiDAR unit frame also prevents gimbal lock in the mounting parameter estimation. This modification is implemented by expressing the term  $R_{Lu}^b$  in (3) as:  $R_{Lu}^b = R_{Lu'}^b R_{Lu'}^{Lu}$ , where  $R_{Lu'}^{Lu}$  is defined according to the laser scanner unit alignment relative to the IMU. The modified LiDAR point positioning is given by the following equation:

$$r_I^m = r_b^m(t) + R_b^m(t) r_{Lu'}^b + R_b^m(t) R_{Lu'}^b R_{Lu'}^{Lu} r_I^{Lu}(t). \quad (4)$$

Since the virtual LiDAR unit frame is almost aligned with the IMU body frame, it results in small values for the differential angular boresight parameters ( $\Delta\omega$ ,  $\Delta\phi$ , and  $\Delta\kappa$ ) relating the two frames. So, the matrix  $R_{Lu'}^b$  can be written as shown in (5), using the small angle approximations. Here,  $\Delta\omega$ ,  $\Delta\phi$ , and  $\Delta\kappa$  denote the rotation around the X-, Y-, and Z-axes of the IMU body frame (i.e., across drive run, along drive run, and vertical directions), respectively. Hence, these parameters denote the boresight pitch, roll, and heading angles, respectively. The point coordinates relative to the virtual LiDAR unit frame are given by (6). These coordinates ( $X'$ ,  $Y'$ , and  $Z'$ ) also denote the location of a point with respect to the vehicle because the virtual LiDAR unit frame is almost parallel to the IMU body frame, which is parallel to the vehicle coordinate system. Substituting (5) and (6) in (4), we get the revised form of the LiDAR point positioning equation, as given in (7), where  $\Delta X$ ,  $\Delta Y$ , and  $\Delta Z$  are the lever-arm offset components of the LiDAR unit frame relative to the IMU body frame

$$R_{Lu'}^b = \begin{bmatrix} 1 & -\Delta\kappa & \Delta\phi \\ \Delta\kappa & 1 & -\Delta\omega \\ -\Delta\phi & \Delta\omega & 1 \end{bmatrix} \quad (5)$$

TABLE I  
IMPACT OF BIAS IN EACH OF THE MOUNTING PARAMETERS  
ON 3-D POINT COORDINATES

	$\delta X_m$	$\delta Y_m$	$\delta Z_m$
$\delta \Delta X$	$\pm \delta \Delta X$	0	0
$\delta \Delta Y$	0	$\pm \delta \Delta Y$	0
$\delta \Delta Z$	0	0	$\delta \Delta Z$
$\delta \Delta \omega$	$\pm y' D\phi \delta \Delta \omega$ $\mp z' \delta \Delta \omega$	$\mp y' D\omega \delta \Delta \omega$	$y' \delta \Delta \omega$ $-z' D\omega \delta \Delta \omega$
$\delta \Delta \phi$	$\pm z' \delta \Delta \phi$ $\mp x' D\phi \delta \Delta \phi$	$\pm x' D\omega \delta \Delta \phi$	$-x' \delta \Delta \phi$ $-z' D\phi \delta \Delta \phi$
$\delta \Delta \kappa$	$\mp y' \delta \Delta \kappa$	$\pm x' \delta \Delta \kappa$	$x' D\omega \delta \Delta \kappa$ $+ y' D\phi \delta \Delta \kappa$

$$r_I^{\text{Lu}'}(t) = R_{\text{Lu}}^{\text{Lu}'} r_I^{\text{Lu}}(t) = \begin{bmatrix} x' \\ y' \\ z' \end{bmatrix} \quad (6)$$

$$r_I^m = r_b^m(t) + R_b^m(t) \begin{bmatrix} \Delta X \\ \Delta Y \\ \Delta Z \end{bmatrix} + R_b^m(t) \begin{bmatrix} 1 & -\Delta \kappa & \Delta \phi \\ \Delta \kappa & 1 & -\Delta \omega \\ -\Delta \phi & \Delta \omega & 1 \end{bmatrix} \begin{bmatrix} x' \\ y' \\ z' \end{bmatrix}. \quad (7)$$

A nearly vertical system implies that the  $Z$ -axis of the IMU body frame is not perfectly aligned with the vertical direction of the mapping frame, i.e., the IMU unit has a slight tilt along and/or across the driving direction. Let these tilt values be denoted by  $D\omega$  and  $D\phi$ , respectively. Moreover, we assume that the drive run directions are either from south-to-north ( $\kappa = 0^\circ$ ) or from north-to-south ( $\kappa = 180^\circ$ ) directions. This assumption facilitates the decision as to whether the impact is along/across the drive run and vertical directions. As a result, the rotation matrix  $R_b^m(t)$  would be given by (8), as shown at the top of the next page, where the top sign is for S-N and bottom sign is for N-S drive run directions. These assumptions would simplify the LiDAR point positioning equation to the form in (9), as shown at the top of the next page. Now, the impact on mapping frame coordinates due to the presence of bias in the system mounting parameters can be analyzed by differentiating (9) with respect to the system mounting parameters. This impact is given by (10), as shown at the top of the next page.

Finally, the bias impact can be studied by isolating the terms in (10) corresponding to the bias in one of the mounting parameters at a time, as given by Table I. Here, the terms  $\delta \Delta X$ ,  $\delta \Delta Y$ ,  $\delta \Delta Z$ ,  $\delta \Delta \omega$ ,  $\delta \Delta \phi$ , and  $\delta \Delta \kappa$  denote the biases in the available values of the mounting parameters:  $\Delta X$ ,  $\Delta Y$ ,  $\Delta Z$ ,  $\Delta \omega$ ,  $\Delta \phi$ , and  $\Delta \kappa$ , respectively. Also,  $\delta X_m$ ,  $\delta Y_m$ , and  $\delta Z_m$  denote the impact on the mapping coordinates:  $X$ ,  $Y$ , and  $Z$ , respectively.

Now, Table I can be used to conduct a bias impact analysis for planar surfaces in different orientations (vertical planes parallel to drive run direction, vertical planes perpendicular to driverun direction and horizontal planes) in order to observe

the impact of each bias on one direction at a time, i.e., in the direction normal to the planes (across drive run direction, along drive run direction, and vertical direction, respectively). The effect of biases on planar surfaces can be quantified by the change in RMSE of plane fitting in the absence and presence of bias in mounting parameters. This change signifies the introduced deformations/discrepancies, which in turn enhances our ability for bias detection and estimation of mounting parameters. There are three different scenarios in terms of the drive run configuration to be considered while evaluating the RMSE: 1) planar points scanned in a single drive run; 2) planar points scanned in two drive runs in same direction; and 3) planar points scanned in two drive runs in opposite directions.

The assessment of the above impacts for different plane orientations and drive run configurations is discussed in more detail in Section II-D. One should note that since the drive run directions are assumed to be either N-S or S-N, and the mapping frame coordinate system is defined such that the  $X$ -,  $Y$ -, and  $Z$ -axes correspond to across drive run, along drive run, and vertical directions, respectively. However, this is only done to simplify the analysis of bias impact.

#### D. Assessment of Bias Impact for Different Plane Orientations and Drive Run Configurations

1) *Impact of Bias in Lever-Arm Component Across the Drive Run Direction ( $\Delta X$ ):* A bias in this component ( $\delta \Delta X$ ) will introduce a constant shift ( $\pm \delta \Delta X$ ) across the drive run direction. The introduced shift is drive run direction dependent. It does not depend on the location of the point in question relative to the laser beam firing point. As a result, the RMSE for all the planes scanned from a single drive run or two drive runs in same direction will remain the same whether or not there is a bias in this parameter. On the other hand, in case of planes scanned from two drive runs in opposite directions, the RMSE will maximally increase for vertical planes parallel to the drive run direction.

2) *Impact of Bias in Lever-Arm Component Along the Drive Run Direction ( $\Delta Y$ ):* A bias in this component ( $\delta \Delta Y$ ) will introduce a constant shift ( $\pm \delta \Delta Y$ ) along the drive run direction. The introduced shift is drive run direction dependent. It does not depend on the location of the point in question relative to the laser beam firing point. Again, the RMSE for all the planes scanned from a single drive run or two drive runs in same direction will remain the same whether or not there is a bias in this parameter. On the other hand, in case of planes scanned from two drive runs in opposite directions, the RMSE will maximally increase for the vertical planes perpendicular to the drive run direction.

3) *Impact of Bias in Lever-Arm Component in the Vertical Direction ( $\Delta Z$ ):* A bias in this component ( $\delta \Delta Z$ ) will introduce a constant shift ( $\delta \Delta Z$ ) in the vertical direction. The introduced shift is drive run direction independent. It does not depend on the location of the point in question relative to the laser beam firing point. As a result, the entire point cloud would be shifted in the vertical direction by the same amount. So, this bias would not affect the RMSE of planes in any of the orientations for any drive run configuration.

$$R_b^m(t) = \begin{bmatrix} \pm 1 & 0 & \pm D\phi \\ 0 & \pm 1 & \mp D\omega \\ -D\phi & D\omega & 1 \end{bmatrix} \quad (8)$$

$$r_I^m = r_b^m(t) + \begin{bmatrix} \pm 1 & 0 & \pm D\phi \\ 0 & \pm 1 & \mp D\omega \\ -D\phi & D\omega & 1 \end{bmatrix} \begin{bmatrix} \Delta X \\ \Delta Y \\ \Delta Z \end{bmatrix} + \begin{bmatrix} \pm 1 & 0 & \pm D\phi \\ 0 & \pm 1 & \mp D\omega \\ -D\phi & D\omega & 1 \end{bmatrix} \begin{bmatrix} 1 & -\Delta\kappa & \Delta\phi \\ \Delta\kappa & 1 & -\Delta\omega \\ -\Delta\phi & \Delta\omega & 1 \end{bmatrix} \begin{bmatrix} x' \\ y' \\ z' \end{bmatrix} \quad (9)$$

$$\delta r_I^m(\delta\Delta X, \delta\Delta Y, \delta\Delta Z, \delta\Delta\omega, \delta\Delta\phi, \delta\Delta\kappa)$$

$$= \begin{bmatrix} \pm\delta\Delta X \\ \pm\delta\Delta Y \\ \delta\Delta Z \end{bmatrix} + \begin{bmatrix} \pm y'D\phi\delta\Delta\omega \pm z'\delta\Delta\phi \mp x'D\phi\delta\Delta\phi \mp y'\delta\Delta\kappa \\ \mp z'\delta\Delta\omega \mp y'D\omega\delta\Delta\omega \pm x'D\omega\delta\Delta\phi \pm x'\delta\Delta\kappa \\ y'\delta\Delta\omega - z'D\omega\delta\Delta\omega - x'\delta\Delta\phi - z'D\phi\delta\Delta\phi + x'D\omega\delta\Delta\kappa + y'D\phi\delta\Delta\kappa \end{bmatrix}. \quad (10)$$

4) *Impact of Bias in Boresight Pitch ( $\Delta\omega$ ):*

1) *Shift across drive run direction:* The impact of boresight pitch bias across the drive run direction ( $\pm y'D\phi\delta\Delta\omega$ ) is  $y'$ -coordinate dependent, i.e., the shift for each point is dependent on its distance along the driving direction from the laser beam firing point. So, all the points belonging to a planar patch will be shifted by different amounts as each point will have a different  $y'$  value depending on the instantaneous location of the vehicle when the point was scanned. This would cause an increase in RMSE of vertical planes parallel to the drive run direction for a single track. However, this increase would be negligible as  $D\phi$  and  $\delta\Delta\omega$  are very small and so, the shift  $y'D\phi\delta\Delta\omega$  would be small unless the  $y'$ -coordinate for the planar points is large enough. Furthermore, the RMSE on combining two tracks in same or opposite directions would depend on the  $\pm y'$  variability within the points comprising the planes.

2) *Shift along drive run direction:* The impact of boresight pitch bias along the drive run direction consists of two terms. The shift caused by the first term ( $\mp z'\delta\Delta\omega$ ) is drive run direction dependent and its magnitude depends on the height ( $z'$ ) of the point in question relative to the laser beam firing point. Whenever the height and boresight pitch bias are small, this impact might be insignificant. In case of vertical planes perpendicular to the drive run direction scanned from a single track, all the points lying at the same height will be shifted by the same amount along the drive run direction, thus resulting in a tilt in the plane. So, the RMSE will not be affected by this term. Similarly, the RMSE will remain the same on combining two tracks in the same direction. But, since this shift is drive run direction dependent, this would result in an increase in RMSE of the planes on combining two tracks in opposite directions.

The second term ( $\mp y'D\omega\delta\Delta\omega$ ) implies that the shift for each point is dependent on its  $y'$ -coordinate. This would cause an increase in RMSE of the planes perpendicular to the drive run direction for a single track. However, this increase would be negligible as  $D\omega$  and  $\delta\Delta\omega$  are very small and so, the shift  $y'D\omega\delta\Delta\omega$  would be small unless the  $y'$ -coordinate for the planar points is large enough. Also, the RMSE on combining two tracks in same or opposite directions would depend on the  $\pm y'$  variability within the points comprising the planes.

3) *Shift in vertical direction:* The impact of boresight pitch bias in the vertical direction also consists of two terms. The shift caused by the first term ( $y'\delta\Delta\omega$ ) depends on the  $y'$ -coordinate of the point in question. So, this would cause an increase in RMSE of the horizontal planes for a single track, which in turn will lead to a large RMSE on combining tracks oriented in same or opposite directions.

The shift caused by the second term ( $-z'D\omega\delta\Delta\omega$ ) is drive run direction independent but depends on the height ( $z'$ ) of the point in question relative to the laser beam firing point. For a horizontal plane,  $z'$ -coordinate of all the points will be almost same. So, this term will not impact the RMSE of horizontal planes for any of the three drive run configurations.

5) *Impact of Bias in Boresight Roll ( $\Delta\phi$ ):*

1) *Shift across drive-run direction:* The impact of this bias across the drive run direction consists of two terms. The shift caused by the first term ( $\pm z'\delta\Delta\phi$ ) is drive run direction dependent and its magnitude depends on the height ( $z'$ ) of the point in question relative to the laser beam firing point. Whenever the height and boresight roll bias are small, this impact might be insignificant. In case of vertical planes parallel to the drive run direction scanned from a single track, all the points lying at the same height will be shifted by the same amount across the drive run direction, thus resulting in a tilt in the plane. So, the RMSE for a single track will not be affected by this term. Similarly, the RMSE will remain the same on combining two tracks in the same direction. But, since this shift is drive run direction dependent, this would result in an increase in RMSE of the planes on combining two tracks in opposite directions.

The shift caused by the second term ( $\mp x'D\phi\delta\Delta\phi$ ) is drive run direction independent since the dual signs will be nullified by  $x'$ , which will also have opposite signs for two tracks in opposite directions. Also, the shift for each point is dependent on its distance across the drive run direction from the laser scanner trajectory ( $x'$ ). However, in case of vertical planes parallel to the drive run direction,  $x'$ -coordinate of all the points will be almost the same. So, the RMSE of such planes will not change for single tracks. However, on combining two tracks (say, A and B) in the same direction, the discrepancy across the drive run direction for a point scanned in the two tracks is given by (11). Similarly, on combining

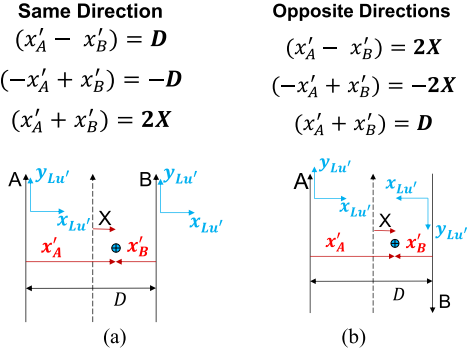


Fig. 2. Relationship between  $x'$ -coordinates for (a) two tracks in the same direction and (b) two tracks in opposite directions.

two tracks in opposite directions, the discrepancy across the drive run direction is given by (12). Referring to Fig. 2, (11) and (12) are simplified to obtain (13), where  $D_{AB}$  denotes the lateral distance between the two tracks. Hence, the RMSE on combining two tracks in same or opposite directions would increase according to the lateral distance between the tracks.

Same Direction:

$$\delta X_{m_A} - \delta X_{m_B} = (-x'_A + x'_B) D\phi\delta\Delta\phi. \quad (11)$$

Opposite Directions :

$$\delta X_{m_A} - \delta X_{m_B} = (-x'_A - x'_B) D\omega\delta\Delta\phi \quad (12)$$

$$\delta X_{m_A} - \delta X_{m_B} = -D_{AB}D\phi\delta\Delta\phi. \quad (13)$$

- 2) *Shift along drive run direction:* The impact of boresight roll bias along the drive run direction ( $\pm x'\delta\omega\delta\Delta\phi$ ) is drive run direction independent. Also, the shift for each point is dependent on its  $x'$ -coordinate. For a vertical plane perpendicular to the drive run direction, all the points which have the same lateral distance will be shifted by the same amount along the drive run direction. This would only cause a tilt in the planar surface and thus, it would not affect its RMSE when dealing with a single drive run. Furthermore, the discrepancies along the drive run direction on combining two tracks in the same direction and in opposite directions are given by (14) and (15), respectively. These equations are simplified according to Fig. 2 to obtain (16). So, it can be concluded that the RMSE on combining two tracks in same or opposite directions would increase according to the lateral distance between the tracks.

Same Direction:

$$\delta Y_{m_A} - \delta Y_{m_B} = (x'_A - x'_B) D\omega\delta\Delta\phi. \quad (14)$$

Opposite Directions:

$$\delta Y_{m_A} - \delta Y_{m_B} = (x'_A + x'_B) D\omega\delta\Delta\phi \quad (15)$$

$$\delta Y_{m_A} - \delta Y_{m_B} = D_{AB}D\omega\delta\Delta\phi. \quad (16)$$

- 3) *Shift in vertical direction:* The impact of this bias in the vertical direction consists of two terms. The shift caused by the first term ( $-x'\delta\Delta\phi$ ) is drive run direction dependent and its magnitude depends on the  $x'$ -coordinate of the point in question. In case of horizontal planes scanned from a single track, all the points located at

the same lateral distance from the track will be shifted vertically by the same amount, thus resulting in a tilt in the plane. So, the RMSE for single tracks will not be affected by this term. Now, using Fig. 2 as reference, the discrepancies in the vertical direction on combining two tracks in the same direction and in opposite directions are given by (17) and (18), respectively. The term  $X$  in (18) denotes the distance of the point from the line bisecting the lateral distance between the two drive runs, as can be seen in Fig. 2. Hence, for two tracks in the same direction, the RMSE will increase according to the lateral distance between the tracks. On the other hand, for two tracks in opposite directions, RMSE will increase depending on the lateral location of the planar patch of interest relative to the bisecting direction between the tracks.

Same Direction:

$$\delta Z_{m_A} - \delta Z_{m_B} = (-x'_A + x'_B)\delta\Delta\phi = -D_{AB}\delta\Delta\phi. \quad (17)$$

Opposite Directions:

$$\delta Z_{m_A} - \delta Z_{m_B} = (-x'_A + x'_B)\delta\Delta\phi = -2X\delta\Delta\phi. \quad (18)$$

The shift caused by the second term ( $-z'\delta\Delta\phi$ ) is drive run direction independent. Also, the shift for each point is dependent on its height ( $z'$ ) relative to the laser beam firing point. For a horizontal plane,  $z'$ -coordinate of all the points will be almost same. So, this term will not impact the RMSE of horizontal planes for any of the three drive run configurations.

#### 6) Impact of Bias in Boresight Heading ( $\Delta\kappa$ ):

- 1) *Shift across drive run direction:* The impact of this bias across the drive run direction ( $\mp y'\delta\Delta\kappa$ ) is  $y'$ -coordinate dependent. So, this would cause an increase in RMSE for the vertical planes parallel to the drive run direction for a single track. Moreover, the RMSE on combining two tracks in same or opposite directions would depend on the  $\pm y'$  variability within the points comprising the planes.

- 2) *Shift along drive run direction:* The impact of this bias along the drive run direction ( $\pm x'\delta\Delta\kappa$ ) is drive run direction independent. Also, the shift for each point is dependent on its  $x'$ -coordinate. However, in case of vertical planes perpendicular to the drive run direction, the RMSE for a single track would not be affected as the presence of this bias would only cause a tilt in the planar surface. Again, referring to Fig. 2, the discrepancies along the drive run direction on combining two tracks in the same direction and in opposite directions are given by (19) and (20), respectively. So, it can be concluded that the RMSE on combining two tracks in same or opposite directions would increase according to the lateral distance between the tracks.

Same Direction:

$$\delta Y_{m_A} - \delta Y_{m_B} = (x'_A - x'_B)\delta\Delta\kappa = D_{AB}\delta\Delta\kappa \quad (19)$$

Opposite Directions:

$$\delta Y_{m_A} - \delta Y_{m_B} = (x'_A + x'_B)\delta\Delta\kappa = D_{AB}\delta\Delta\kappa. \quad (20)$$

- 3) *Shift in vertical direction:* The impact of this bias in the vertical direction consists of two terms. The

TABLE II  
POTENTIAL IMPACT ON RMSE OF PLANE FITTING BASED ON THE THEORETICAL BIAS IMPACT ANALYSIS

Bias Type	Plane Orientation	Vertical & Parallel to Drive-run Direction	Vertical & Perpendicular to Drive-run Direction	Horizontal Planes
		Across Drive-run Direction	Along Drive-run Direction	Vertical Direction
	Drive-run Configuration			
$\delta\Delta X$	Single Track	Same	Same	Same
	Two tracks (Same direction)	Same	Same	Same
	Two tracks (Opposite directions)	Increase	Same	Same
$\delta\Delta Y$	Single Track	Same	Same	Same
	Two tracks (Same direction)	Same	Same	Same
	Two tracks (Opposite directions)	Same	Increase	Same
$\delta\Delta Z$	Single Track	Same	Same	Same
	Two tracks (Same direction)	Same	Same	Same
	Two tracks (Opposite directions)	Same	Same	Same
$\delta\Delta \omega$	Single Track	Might increase	Might increase	Increase
	Two tracks (Same direction)	Might increase	Might increase	Increase
	Two tracks (Opposite directions)	Might increase	Increase	Increase
$\delta\Delta \phi$	Single Track	Same	Same	Same
	Two tracks (Same direction)	Increase	Increase	Increase
	Two tracks (Opposite directions)	Increase	Increase	Increase
$\delta\Delta \kappa$	Single Track	Increase	Same	Same
	Two tracks (Same direction)	Increase	Increase	Increase
	Two tracks (Opposite directions)	Increase	Increase	Increase

shift caused by the first term ( $x'D\omega\delta\Delta\kappa$ ) is drive run direction dependent and its magnitude depends on the  $x'$ -coordinate of the point in question. In case of horizontal planes scanned from a single track, all the points located at the same lateral distance from the track will be shifted vertically by the same amount, thus resulting in a tilt in the plane. So, the RMSE for single tracks will not be affected by this term. Now, according to Fig. 2, the discrepancies along the drive run direction on combining two tracks in the same direction and in opposite directions are given by (21) and (22), respectively. Hence, for two tracks in the same direction, the RMSE will increase according to the lateral distance between the tracks. On the other hand, for two tracks in opposite directions, RMSE will increase depending on the extent of the lateral distance variability of the planar patch of interest relative to the bisecting direction between the tracks.

Same Direction:

$$\delta Z_{m_A} - \delta Z_{m_B} = (x'_A - x'_B) D\omega\delta\Delta\kappa = D_{AB} D\omega\delta\Delta\kappa \quad (21)$$

Opposite Directions:

$$\delta Z_{m_A} - \delta Z_{m_B} = (x'_A - x'_B) D\omega\delta\Delta\kappa = 2X D\omega\delta\Delta\kappa. \quad (22)$$

Now, the shift caused by the second term ( $y'D\phi\delta\Delta\kappa$ ) is  $y'$ -coordinate dependent. So, this would cause an increase in RMSE of the horizontal planes for a single track, which in turn will lead to an increase in RMSE on combining tracks oriented in same or opposite directions. However, this increase would be negligible as  $D\phi$  and  $\delta\Delta\kappa$  are very small and so, the shift  $y'D\phi\delta\Delta\kappa$  would be small unless the  $y'$ -coordinate for the planar points is large enough.

Note that throughout the above discussion, we refer to the coordinates or bias values being “small” or “large enough.”

In this context, a coordinate or bias is considered “small” if its impact on the point cloud lies within the limits of the expected accuracy in point positioning according to the specifications of the hardware components included in the mobile mapping system, i.e., the LiDAR and GNSS/INS units. Similarly, a coordinate or bias is considered “large enough” if the resultant bias impact is beyond the expected accuracy in point positioning.

Table II summarizes the above discussion by listing whether the RMSE of plane fitting on introducing a bias in mounting parameters ( $\text{RMSE}_{\text{Bias}}$ ) would potentially increase or remain the same as compared to the RMSE from the original point cloud ( $\text{RMSE}_{\text{True}}$ ) for different plane orientations and drive run configurations in case of a nearly vertical system.

The above analysis can be used to draw conclusions about the target primitives and drive run configurations required to estimate each mounting parameter.

- 1) The lever arm  $\Delta X$  can be estimated using opposite drive runs while scanning vertical planar features parallel to the drive run direction.
- 2) The lever arm  $\Delta Y$  can be estimated using opposite drive runs while scanning vertical planar features perpendicular to the drive run direction.
- 3) The lever arm  $\Delta Z$  for a given spinning multibeam laser scanner can be estimated only using vertical control.
- 4) The boresight pitch ( $\Delta\omega$ ) can be estimated using horizontal planar features in addition to using two opposite drive runs while scanning vertical planar features perpendicular to the drive run direction. The height of the planar features is critical to decouple this parameter from the lever-arm component ( $\Delta Y$ ).
- 5) The boresight roll ( $\Delta\phi$ ) can be estimated using two opposite drive runs while scanning vertical planar features parallel to the drive run direction. The height of the

planar features is critical to decouple this parameter from the lever-arm component ( $\Delta X$ ). The setup should also include horizontal planar features scanned from opposite drive runs at different lateral distances from the features and scanned from drive runs in the same direction but with different lateral separations.

- 6) The boresight heading ( $\Delta\kappa$ ) can be estimated by scanning vertical planes from two drive runs in the same direction with a significant lateral separation between them. This configuration would eliminate any discrepancies caused by lever-arm components. This setup should also include horizontal planar features scanned from opposite drive runs at different lateral distances from the features and scanned from drive runs in the same direction but with different lateral separations.

### III. PROPOSED MULTIUNIT LiDAR SYSTEM CALIBRATION PROCEDURE

In this section, we propose a strategy to calibrate the mounting parameters using geometric tie features (e.g., planar, and linear/cylindrical features). After collecting data from several drive runs, a 3-D point cloud relative to a global reference frame will be derived using the GNSS/INS unit position and orientation, and initial estimates for the mounting parameters. Then, conjugate features are identified and extracted from the reconstructed point cloud. Finally, an iterative multiunit system calibration with weight modification is proposed to derive the mounting parameters based on the minimization of normal distance between conjugate features.

The mounting parameters that are derived in multisensor calibration are the lever arm ( $\Delta X$  and  $\Delta Y$ ) and boresight angles ( $\Delta\omega$ ,  $\Delta\phi$ , and  $\Delta\kappa$ ) for all the sensors and the lever arm  $\Delta Z$  for all but the reference sensor. The lever arm  $\Delta Z$  for the reference sensor cannot be estimated in the calibration procedure since any change in  $\Delta Z$  will not introduce discrepancies among the different versions of the same feature captured from different sensors and/or drive runs. It would only result in a shift of the point cloud in the vertical direction as a whole. So,  $\Delta Z$  for the reference sensor is fixed during the calibration procedure. It is either manually measured or determined using vertical control (such as, horizontal planar patches with known elevation).

#### A. Feature Extraction

The conceptual basis for multiunit LiDAR system calibration is to minimize the discrepancies among conjugate points, linear features, and/or planar features obtained from different sensors and/or drive runs. Owing to the irregular distribution of LiDAR points, conjugate point pairs cannot be used since there is no accurate point-to-point correspondence. Instead, conjugate linear/cylindrical and planar features, such as building façades, ground patches, light poles, and lane markers, are used and these can be directly extracted from overlapping areas within the drive runs. However, conjugate feature extraction from several drive runs could be time-consuming and inefficient, especially when the initial estimates for mounting parameters used to reconstruct the 3-D point

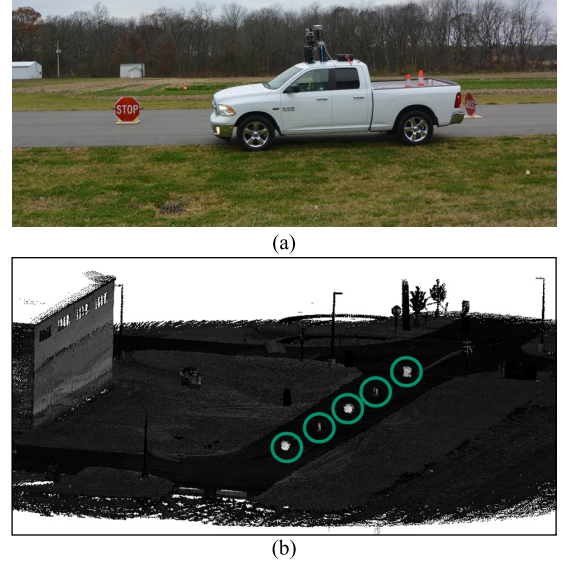


Fig. 3. (a) Calibration test-field and data collection system. (b) Intensity data of a point cloud obtained from a single drive run.

cloud are considerably inaccurate. To facilitate automated identification of conjugate features in such cases, specifically designed calibration boards covered by highly reflective surfaces that could be easily deployed and set up in outdoor environments, are used in this paper, as shown in Fig. 3(a). In this paper, various traffic signs (75 cm wide stop signs and 90 cm  $\times$  60 cm wrong way signs) are used as highly reflective boards.

The highly reflective boards can be easily identified from intensity data, as in Fig. 3(b) (green circles), where the points belonging to these boards exhibit higher intensity values compared to other LiDAR points. First, a predefined threshold ( $I_{th}$ ) is set to extract high-intensity points. To avoid the extraction of high-intensity points belonging to objects other than these boards, an approximate location is manually set as a seed point for each board captured in all the tracks. Then, for each of the tracks, a distance-based region growing technique is adopted to group the high-intensity points belonging to these boards starting from the preset seed point. The distance threshold ( $d_{th}$ ) used for region growing is determined based on the accuracy of initial estimates of the mounting parameters. Finally, a plane fitting is done for these points from each track, and the points lying within a normal distance threshold ( $nd_{th}$ ) from the best-fitting plane are extracted. Other planar features, such as ground patches or wall patches, can be extracted by defining two diagonally opposite corners. A bounding box is constructed around the planar feature of interest by adding a buffer value ( $bf$ ) in  $x$ -,  $y$ -, and  $z$ -directions to the coordinates of diagonally opposite corners. Again, a plane fitting is done for the points contained inside the box, and the ones lying within a normal distance threshold ( $nd_{th}$ ) from the best-fitting plane are extracted. Linear/cylindrical features can also be used for calibration and they are extracted by specifying the two end points for each feature. A buffer radius ( $bf$ ) is set to define a cylinder around the linear/cylindrical feature of interest. Then, a line/cylinder fitting is done for the points

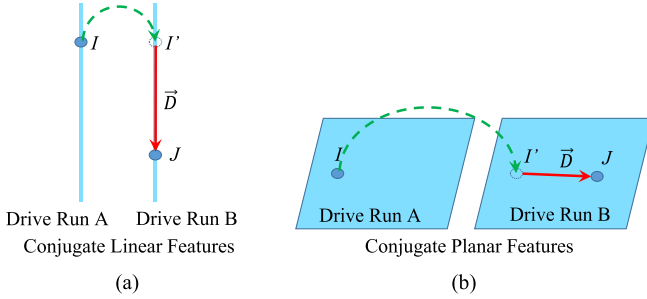


Fig. 4. Discrepancy vector between nonconjugate points along corresponding (a) linear and (b) planar features.

lying within this cylindrical buffer and finally, the points that lie within a normal distance threshold ( $nd_{th}$ ) from the best-fitting line/cylinder are extracted. Note that the buffer value (bf) and the normal distance threshold ( $nd_{th}$ ) for planar and linear/cylindrical features are determined based on the accuracy of initial estimates of the mounting parameters.

#### B. Weight Modification and Multisensor System Calibration

In the proposed calibration method, conjugate features are extracted from the point clouds of different sensors and several drive runs. The mounting parameters of each sensor are derived by minimizing the discrepancies among conjugate features (points/lines/planes) in overlapping drive runs. Each pairing between conjugate features will result in a misclosure vector, which would be random ( $\vec{e}$ ) in case of a conjugate point pair, as given by (23). However, a pairing between nonconjugate points along corresponding planar or linear/cylindrical features would additionally introduce a nonrandom component ( $\vec{D}$ ) in the misclosure vector, as given by (24). This  $\vec{D}$  would lie along the planar surface or along the linear feature/axis of cylinder, respectively, as illustrated in Fig. 4. Therefore, a modified weight matrix,  $P'$ , is introduced to eliminate the nonrandom component of the misclosure vector,  $\vec{D}$ , from the LSA cost function, as given by (25) [17]. To derive this matrix, a local coordinate system ( $UVW$ ) is established first. For linear/cylindrical features, the  $U$ -axis is aligned along the line/axis of cylinder and  $V$ - and  $W$ -axes are arbitrarily chosen to satisfy the orthogonality of the  $UVW$  triad. For planar features,  $W$ -axis is aligned along the normal vector of the plane in question, and  $U$ - and  $V$ -axes are arbitrarily chosen along the planar feature. An illustration of the local coordinate systems for the two types of features is shown in Fig. 5. Then, a rotation matrix,  $R_{XYZ}^{UVW}$ , relating the local and mapping coordinate systems is derived according to the components of the vectors,  $U$ ,  $V$ , and  $W$  relative to the mapping frame. The weight matrix,  $P_{XYZ}$ , in the mapping coordinate system is transformed to a weight matrix,  $P_{UVW}$ , in the local coordinate system according to the law of error propagation (26). The weight matrix,  $P_{UVW}$ , is modified by assigning a zero weight to the elements corresponding to the direction of  $\vec{D}$ . More specifically, the nonrandom component of the misclosure vector ( $\vec{D}$ ) can be eliminated from the LSA minimization target function by setting a zero weight in the corresponding direction. The direction of ( $\vec{D}$ ) for a linear/cylindrical feature

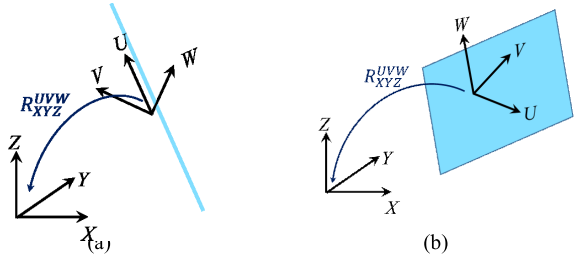


Fig. 5. Illustration of local coordinate systems for (a) linear and (b) planar features.

is along the  $U$ -axis. Therefore, the modified weight matrix,  $P'_{UVW}$ , has zero weight in all the elements pertaining to the  $U$ -axis (27). Similarly, the direction of ( $\vec{D}$ ) for a planar feature is along the  $U$ - and  $V$ -axes. So, all the elements pertaining to the  $U$ - and  $V$ -axes are assigned a zero weight (28). The modified weight matrix,  $P'_{XYZ}$ , in the mapping coordinate system is derived using (29). Finally, the obtained modified weight matrix,  $P'_{XYZ}$ , is applied to the condition in (24) to account for nonconjugate points along corresponding features within overlapping drive runs

$$\text{Points: } r_I^m(\text{drive run 1}) - r_I^m(\text{drive run 2}) = \vec{e}. \quad (23)$$

$$\begin{aligned} \text{Linear/Planar Features: } r_I^m(\text{drive run 1}) - r_J^m(\text{drive run 2}) \\ = \vec{D} + \vec{e} \end{aligned} \quad (24)$$

$$P'\vec{D} = P' \begin{bmatrix} d_x \\ d_y \\ d_z \end{bmatrix} = 0 \quad (25)$$

$$P_{UVW} = R_{XYZ}^{UVW} P_{XYZ} R_{XYZ}^{UVW T} = \begin{bmatrix} P_U & P_{UV} & P_{UW} \\ P_{VU} & P_V & P_{VW} \\ P_{WU} & P_{WV} & P_W \end{bmatrix} \quad (26)$$

$$\text{Linear/Cylindrical Feature: } P'_{UVW} = \begin{bmatrix} 0 & 0 & 0 \\ 0 & P_V & P_{VW} \\ 0 & P_{WV} & P_W \end{bmatrix} \quad (27)$$

$$\text{Planar Feature: } P'_{UVW} = \begin{bmatrix} 0 & 0 & 0 \\ 0 & 0 & 0 \\ 0 & 0 & P_W \end{bmatrix} \quad (28)$$

$$P'_{XYZ} = R_{XYZ}^{UVW T} P'_{UVW} R_{XYZ}^{UVW}. \quad (29)$$

The discrepancies among conjugate features from multiple drive runs are used for estimating the system mounting parameters. Every sensor and every drive run will lead to a new version for each feature. For instance, a feature extracted from  $m$  different sensors and  $n$  different drive runs will lead to  $mn$  separate versions for this feature. Then, there can be a total of  $(mn(mn - 1)/2)$  pairings for each feature. However, the discrepancy observations corresponding to these pairings will not be independent. Hence, in this paper, one of the versions is selected as reference to be paired with all the other versions of that feature from other sensors and/or drive runs. So, there would be  $(mn - 1)$  linearly independent pairings for each feature. The version with the maximum number of points belonging to a feature is used as the reference because this will be used to derive the modified weight matrix for that

feature. So, an increased number of points would increase the redundancy of plane or line/cylinder fitting for the feature, thus resulting in a more accurate estimate of the modified weight matrix. Finally, the mounting parameters for both reference and slave laser units can be derived by minimizing the discrepancies among the conjugate features arising from the above mentioned pairs.

However, when the initial estimate of the mounting parameters is inaccurate, the estimated modified weight matrix would be imprecise which would affect the accuracy of the derived mounting parameters. Hence, this paper proposes an iterative calibration procedure. First, the discrepancy among extracted features is minimized to derive mounting parameters through the weight modification process. Then, the points along the extracted features are regenerated using the newly estimated mounting parameters and the discrepancy among conjugate features is minimized again using a newly defined modified weight matrix. The above steps are repeated until the change in the estimates of the mounting parameters is below a predefined threshold.

#### IV. EXPERIMENTAL RESULTS

##### A. System Integration and Synchronization Process

In this paper, a car-mount system is used to collect LiDAR data for 3-D point cloud reconstruction. In this regard, system integration is considered one of the factors that have a significant effect on the ability to provide accurate geospatial information. This system consists of two LiDAR sensors (Velodyne HDL-32E and VLP-16), and a direct georeferencing unit based on an integrated INS and GNSS receiver boards (SPAN-CPT). All these components are rigidly fixed within the car-mount system. The range accuracies of Velodyne HDL-32E and VLP-16 are 2 and 3 cm, respectively [18], [19]. Also, for SPAN-CPT, the postprocessing accuracy in position can be less than 2 cm and the achieved accuracy for the roll/pitch and heading can be  $0.015^\circ$  and  $0.08^\circ$ , respectively [20]. These values suggest that we should expect a similar accuracy (around 3 cm) for the proposed calibration procedure.

In order to derive direct georeferencing data, the SPAN-CPT supplies sequentially precise time pulses, known as pulse-per-second signals, which give the ability to generate a time-tagged point cloud. Furthermore, the SPAN-CPT provides a navigation message, also known as GPRMC message (including information regarding position, rotation, and GPS time), which is recorded over a dedicated RS-232 serial port and received by the LiDAR unit via the interface box in the form of serial data. This synchronization process is illustrated in Fig. 6.

##### B. Experimental Verification of Bias Impact Analysis

The numerical verification of the theoretical impact is done by first, extracting vertical planes that are parallel or perpendicular to the drive run direction, and horizontal planes from a point cloud obtained using a precalibrated system that is assumed to have no biases in the system mounting parameters. Then, the RMSE values are evaluated to describe the quality of fit for these planes before adding biases to the system mounting parameters. Next, a bias is introduced in

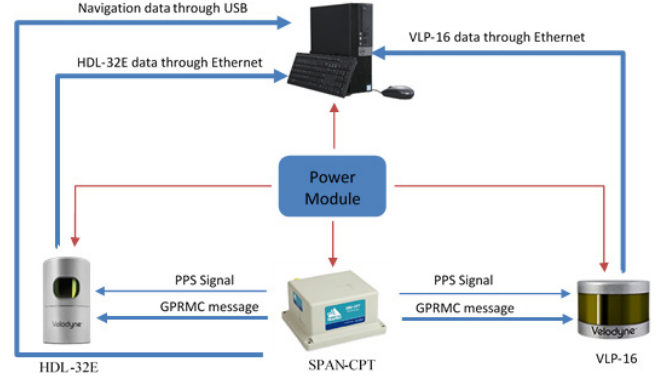


Fig. 6. Synchronization process and data storage for the terrestrial mobile mapping system.



Fig. 7. Drive run configurations used for bias impact analysis.

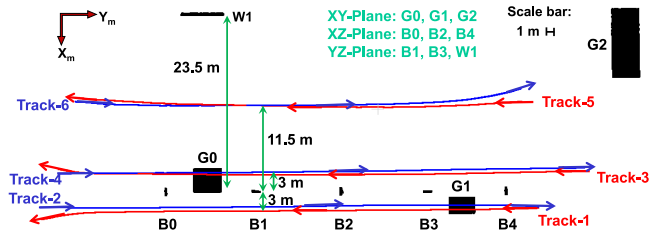


Fig. 8. Target primitives and drive runs used for bias impact analysis.

the system mounting parameters, one by one, and the point clouds are reconstructed for each case. For this paper, the bias introduced in the lever-arm components is 20 cm, and the bias introduced in the boresight angles is 120 arc-min. Finally, the RMSE values for the planar features are estimated for the individual drive runs as well as combined drive runs with different configurations. These values are compared with the original RMSE values to verify our hypotheses about the impact of various biases in the system mounting parameters. Four different drive run configurations are used for this paper: a pair of drive runs in the same direction and opposite directions at two different lateral distances for each case. This is schematically shown in Fig. 7. The target primitives and the relative location of the drive runs that are used to observe the impact of biases are depicted in Fig. 8, along with the orientation of these calibration primitives relative to the drive runs. Here, G0~G2 are ground patches, B0~B4 are highly reflective sign boards, and W1 is a wall patch. The orientation of mapping frame is also indicated in the top left corner of Fig. 8 as  $X_m$  and  $Y_m$ .

Tables III–V list the RMSE of plane fitting (in meters) for one target primitive in each of the three orientations (XY, YZ, and XZ) for the four drive run configurations. The RMSE

TABLE III

BIAS IMPACT ON A VERTICAL PLANE PARALLEL TO DRIVE RUN DIRECTION (YZ PLANE): WALL PATCH (W1)

		RMSE (m)			
		Same direction C1 (1,3) C3 (1,5)		Opposite directions C2 (2,3) C4 (1,6)	
<b>NoBias</b>	Track A	<b>0.0259</b>	<b>0.0259</b>	<b>0.0152</b>	<b>0.0259</b>
	Track B	<b>0.0158</b>	<b>0.0154</b>	<b>0.0158</b>	<b>0.0379</b>
	Combined	<b>0.0206</b>	<b>0.0176</b>	<b>0.0158</b>	<b>0.0351</b>
<b><math>\delta\Delta X</math></b>	Track A	0.0258	0.0258	0.0152	0.0258
	Track B	0.0158	0.0153	0.0158	0.0381
	Combined	0.0206	0.0175	<b>0.1451</b>	<b>0.1845</b>
<b><math>\delta\Delta Y</math></b>	Track A	0.0248	0.0248	0.0152	0.0248
	Track B	0.0167	0.0148	0.0167	0.0426
	Combined	0.0204	0.0178	0.0178	0.0388
<b><math>\delta\Delta Z</math></b>	Track A	0.0254	0.0254	0.0151	0.0254
	Track B	0.0168	0.0158	0.0168	0.0377
	Combined	0.0208	0.0195	0.0166	0.0381
<b><math>\delta\Delta\omega</math></b>	Track A	<b>0.0194</b>	<b>0.0194</b>	<b>0.0152</b>	<b>0.0194</b>
	Track B	<b>0.0126</b>	<b>0.0255</b>	<b>0.0126</b>	<b>0.0709</b>
	Combined	<b>0.0162</b>	<b>0.0248</b>	<b>0.0131</b>	<b>0.0620</b>
<b><math>\delta\Delta\phi</math></b>	Track A	0.0300	0.0300	0.0408	0.0300
	Track B	0.0452	<b>0.0624</b>	0.0452	<b>0.0918</b>
	Combined	<b>0.0399</b>	<b>0.0584</b>	<b>0.0532</b>	<b>0.0858</b>
<b><math>\delta\Delta\kappa</math></b>	Track A	<b>0.3099</b>	<b>0.3099</b>	<b>0.1978</b>	<b>0.3099</b>
	Track B	<b>0.3120</b>	<b>0.3109</b>	<b>0.3120</b>	<b>0.2969</b>
	Combined	<b>0.3124</b>	<b>0.3108</b>	<b>0.3088</b>	<b>0.3008</b>

TABLE IV

BIAS IMPACT ON A VERTICAL PLANE PERPENDICULAR TO DRIVE RUN DIRECTION (XZ PLANE): SIGN BOARD (B0)

		RMSE (m)			
		Same direction C1 (1,3) C3 (1,5)		Opposite directions C2 (2,3) C4 (1,6)	
<b>NoBias</b>	Track A	<b>0.0097</b>	<b>0.0097</b>	<b>0.0132</b>	<b>0.0097</b>
	Track B	<b>0.0133</b>	<b>0.0076</b>	<b>0.0133</b>	<b>0.0134</b>
	Combined	<b>0.0151</b>	<b>0.0098</b>	<b>0.0187</b>	<b>0.0120</b>
<b><math>\delta\Delta X</math></b>	Track A	0.0144	0.0144	0.0123	0.0144
	Track B	0.0136	0.0087	0.0136	0.0172
	Combined	0.0191	0.0140	0.0168	0.0158
<b><math>\delta\Delta Y</math></b>	Track A	0.0095	0.0095	0.0131	0.0095
	Track B	0.0133	0.0076	0.0133	0.0131
	Combined	0.0150	0.0096	<b>0.1765</b>	<b>0.1557</b>
<b><math>\delta\Delta Z</math></b>	Track A	0.0098	0.0098	0.0130	0.0098
	Track B	0.0134	0.0075	0.0134	0.0169
	Combined	0.0153	0.0099	0.0132	0.0133
<b><math>\delta\Delta\omega</math></b>	Track A	<b>0.0168</b>	<b>0.0168</b>	<b>0.0229</b>	<b>0.0168</b>
	Track B	<b>0.0164</b>	<b>0.0142</b>	<b>0.0164</b>	<b>0.0210</b>
	Combined	<b>0.0195</b>	<b>0.0200</b>	<b>0.0640</b>	<b>0.0422</b>
<b><math>\delta\Delta\phi</math></b>	Track A	0.0092	0.0092	0.0134	0.0092
	Track B	0.0129	0.0107	0.0129	0.0135
	Combined	<b>0.0110</b>	<b>0.0160</b>	<b>0.0135</b>	<b>0.0388</b>
<b><math>\delta\Delta\kappa</math></b>	Track A	0.0145	0.0145	0.0185	0.0145
	Track B	0.0189	0.0212	0.0189	0.0145
	Combined	<b>0.0966</b>	<b>0.1618</b>	<b>0.1022</b>	<b>0.1649</b>

is listed for each track separately (where Track A denotes the first track and Track B denotes the second track in the corresponding configuration) as well as for the two tracks combined together. The values highlighted in light gray denote the ones which can be expected to have a potential increase in RMSE according to the theoretical analysis.

TABLE V

BIAS IMPACT ON A HORIZONTAL PLANE (XY PLANE): GROUND PATCH (G2)

		RMSE (m)			
		Same direction C1 (1,3) C3 (1,5)		Opposite directions C2 (2,3) C4 (1,6)	
<b>NoBias</b>	Track A	<b>0.0156</b>	<b>0.0156</b>	<b>0.0166</b>	<b>0.0156</b>
	Track B	<b>0.0160</b>	<b>0.0154</b>	<b>0.0160</b>	<b>0.0138</b>
	Combined	<b>0.0160</b>	<b>0.0154</b>	<b>0.0176</b>	<b>0.0164</b>
<b><math>\delta\Delta X</math></b>	Track A	0.0153	0.0153	0.0170	0.0153
	Track B	0.0161	0.0175	0.0161	0.0161
	Combined	0.0160	0.0181	0.0194	0.0172
<b><math>\delta\Delta Y</math></b>	Track A	0.0153	0.0153	0.0167	0.0153
	Track B	0.0161	0.0157	0.0161	0.0141
	Combined	0.0160	0.0156	0.0194	0.0187
<b><math>\delta\Delta Z</math></b>	Track A	0.0155	0.0155	0.0166	0.0155
	Track B	0.0160	0.0153	0.0160	0.0139
	Combined	0.0160	0.0153	0.0177	0.0165
<b><math>\delta\Delta\omega</math></b>	Track A	<b>0.0792</b>	<b>0.0792</b>	<b>0.1754</b>	<b>0.0792</b>
	Track B	<b>0.2229</b>	<b>0.1240</b>	<b>0.2229</b>	<b>0.1240</b>
	Combined	<b>0.2323</b>	<b>0.1177</b>	<b>0.3733</b>	<b>0.5391</b>
<b><math>\delta\Delta\phi</math></b>	Track A	0.0353	0.0353	0.0227	0.0353
	Track B	0.0187	0.0312	0.0187	0.0386
	Combined	<b>0.0548</b>	<b>0.1832</b>	<b>0.4916</b>	<b>0.3369</b>
<b><math>\delta\Delta\kappa</math></b>	Track A	0.0156	0.0156	0.0159	0.0156
	Track B	0.0185	0.0304	0.0185	0.0368
	Combined	<b>0.0230</b>	<b>0.0600</b>	<b>0.0953</b>	<b>0.1032</b>

It is worth mentioning that the other target primitives were also observed to exhibit the same trends as the one which is oriented in the same direction, i.e., each of the feature sets—(B1, B3, W1); (B0, B2, B4); and (G0, G1, G2)—displayed the same characteristics. Table III indicates that vertical planes parallel to the drive run direction would aid in estimating  $\Delta X$ ,  $\Delta\phi$ , and  $\Delta\kappa$ , along with a relatively weaker contribution toward  $\Delta\omega$ . The values highlighted in dark gray in Table III indicate a significant increase in the RMSE for Tracks 5 and 6. However, this is not expected theoretically. This is attributed to the points of the planar patch that are captured toward the curved ends of the trajectories, thus leading to a significant change in their  $x'$ -coordinates, which is otherwise assumed to be constant in case of straight tracks capturing such patches. Table IV indicates that vertical planes perpendicular to the drive run direction would facilitate the estimation of  $\Delta Y$ ,  $\Delta\omega$ , and  $\Delta\kappa$ , along with a weaker contribution toward  $\Delta\phi$ . Also, Table V indicates that horizontal planes would indeed help in estimating  $\Delta\omega$  and  $\Delta\phi$ , along with a lesser contribution toward  $\Delta\kappa$ . These results validate the theoretically drawn conclusions about bias impact. So, for proceeding with the calibration of a GNSS/INS-assisted multi-LiDAR unit system, the test field and drive run configurations are set up while taking these results of bias impact analysis into consideration. This is described in more detail in Section IV-C.

#### C. Data Set Description and Multiunit LiDAR System Calibration Results

As mentioned before, the data set used for evaluating the performance of the proposed calibration strategy is captured by

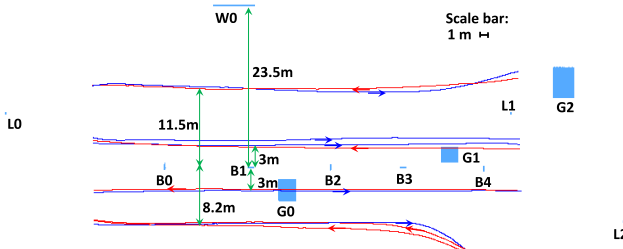


Fig. 9. Configuration of drive runs and calibration boards.

a designed platform which carries a Velodyne HDL-32E and a Velodyne VLP-16 laser scanner together with a SPAN-CPT direct georeferencing unit. Five specially designed highly reflective boards are installed, perpendicular to each other, in a sufficiently spacious area to drive around them. The distance between adjacent sign boards was approximately 10 m along the driving direction. We suggest that the separation between target primitives during calibration should be such that none of the target primitives are highly occluded by the others with respect to the laser scanner. The highly reflective boards, along with the ground patches and light poles, would ensure enough control along all the directions (i.e.,  $x$ -,  $y$ -, and  $z$ -directions). In this experiment, 10 drive runs, with different directions and a lateral separation of approximately 7 m, were made around the calibration primitives at an approximate speed of 4 miles/h. A slow driving speed is recommended to ensure sufficient point density along different features used for calibration, which would enhance the accuracy of calibration results. In this case, the average point density for all the calibration targets was 35 443 points/m<sup>2</sup>. With 10 drive runs and two laser units, we will have a total of 20 versions for each of the features used for the calibration procedure. The configuration of drive runs and boards are shown in Fig. 9. Here, G0~G2 are ground patches, B0~B4 are highly reflective sign boards, L0~L2 are light poles, and W0 is a wall patch. Note that this configuration is in accordance with the optimal drive run and target primitive configurations suggested by the previously conducted bias impact analysis. Here, the HDL-32E and VLP-16 scanners are taken as reference and slave units, respectively. First, all the points are reconstructed using initial estimates of the mounting parameters, which are obtained from manual measurements/estimates for the lever-arm and boresight angles between SPAN-CPT and reference laser unit, and between the reference and slave laser units. Then, the semiautomatic feature extraction is executed to obtain the points for planar features (i.e., specially designed boards and ground patches) and for linear/cylindrical features (i.e., light poles) from all the data sets separately. The average intensity value for the points belonging to the highly reflective sign boards is roughly 150. In this case, the intensity threshold is set as 100 for VLP-16 and 120 for HDL-32E sensors. Increasing these intensity thresholds would result in a reduced number of points extracted along the boards. However, it is worth mentioning that several tests were conducted with different threshold values in the range of 100–150 and it was observed to have negligible impact on the calibration results. The same

TABLE VI  
MOUNTING PARAMETERS OF HDL-32E AND VLP-16 BEFORE  
AND AFTER MULTISENSOR CALIBRATION

HDL-32 LiDAR Unit Mounting Parameters ( $r_{HDL32E}^b$ ) ( $R_{HDL32E}^b$ )						
	$\Delta X$ (m)	$\Delta Y$ (m)	$\Delta Z$ (m)	$\Delta \omega$ (deg)	$\Delta \phi$ (deg)	$\Delta \kappa$ (deg)
Initial	0.4	0.1	0.3	-5	0	-60
Final	0.473	0.195	0.3	-6.089	-0.136	-58.822
Standard Deviation	0.0036	0.0047	0	0.0110	0.0106	0.0088
VLP-16 LiDAR Unit Mounting Parameters ( $r_{VLP16}^{HDL32E}$ ) ( $R_{VLP16}^{HDL32E}$ )						
	$\Delta X$ (m)	$\Delta Y$ (m)	$\Delta Z$ (m)	$\Delta \omega$ (deg)	$\Delta \phi$ (deg)	$\Delta \kappa$ (deg)
Initial	-0.152	-0.259	-0.020	-2.505	-4.329	29.905
Final	-0.239	-0.387	-0.077	-1.638	-4.249	26.776
Standard Deviation	0.0065	0.0058	0.0070	0.0162	0.0171	0.0122

intensity threshold values can be used for any data collection as it is only dependent on the reflectivity of the boards. Since the initial estimates of the mounting parameters are inaccurate, the distance threshold for region growing from the approximate seed points for the boards is set as 0.50 m in order to account for the shift between the different versions of the boards due to the presence of biases. Similarly, the normal distance threshold is set to be 0.30 m and the buffer radius of cylinder/buffer height of bounding box for linear/planar features, respectively, is 0.30 m. These thresholds can be decreased to as low as 0.05–0.10 m in case of relatively accurate initial estimates of mounting parameters. All the above distance thresholds/buffer values are independent of point density and scan characteristics, and can be readjusted for each data collection solely based on the accuracy of initial estimates of the mounting parameters. Finally, the proposed multi-LiDAR unit calibration procedure is applied to obtain the mounting parameters for both the sensors simultaneously, using point pairs from conjugate features in the HDL-32E and VLP-16 data sets. The accuracy of calibration procedure is evaluated by monitoring the *a posteriori* variance factor after every iteration of the LSA procedure and also, the RMSE of the normal distance of points belonging to a planar or linear/cylindrical feature from its best-fitting plane or line, respectively.

The initial approximations of these mounting parameters and the final results from the multisensor calibration for HDL-32E as well as VLP-16 sensors are listed in Table VI. The standard deviations of these parameters (also listed in Table VI) are derived by computing the square root of the diagonal elements of the covariance matrix,  $\Sigma$  for the nonlinear LSA problem [21]. One should note that the lever arm  $\Delta Z$  for the reference sensor (here, HDL-32E) is fixed during the calibration procedure. The correlation matrix for

TABLE VII  
CORRELATION MATRIX OF MOUNTING PARAMETER ESTIMATES FROM MULTISENSOR CALIBRATION

	$\Delta X_1$	$\Delta Y_1$	$\Delta Z_1$	$\Delta \omega_1$	$\Delta \phi_1$	$\Delta \kappa_1$	$\Delta X_2$	$\Delta Y_2$	$\Delta Z_2$	$\Delta \omega_2$	$\Delta \phi_2$	$\Delta \kappa_2$
$\Delta X_1$	1.000	0.044	<b>0.000</b>	0.040	0.226	0.415	0.187	0.367	0.002	0.079	0.062	0.277
$\Delta Y_1$	0.044	1.000	<b>0.000</b>	0.183	0.040	0.132	0.386	0.276	0.123	0.037	0.017	0.071
$\Delta Z_1$	<b>0.000</b>	<b>0.000</b>	<b>0.000</b>	<b>0.000</b>	<b>0.000</b>	<b>0.000</b>	<b>0.000</b>	<b>0.000</b>	<b>0.000</b>	<b>0.000</b>	<b>0.000</b>	<b>0.000</b>
$\Delta \omega_1$	0.040	0.183	<b>0.000</b>	1.000	0.107	0.072	0.013	0.002	0.316	0.156	0.141	0.024
$\Delta \phi_1$	0.226	0.040	<b>0.000</b>	0.107	1.000	0.157	0.011	0.066	0.175	0.371	0.099	0.081
$\Delta \kappa_1$	0.415	0.132	<b>0.000</b>	0.072	0.157	1.000	0.104	0.082	0.082	0.058	0.041	0.517
$\Delta X_2$	0.187	0.386	<b>0.000</b>	0.013	0.011	0.104	1.000	0.489	0.060	0.052	0.092	0.018
$\Delta Y_2$	0.367	0.276	<b>0.000</b>	0.002	0.066	0.082	0.489	1.000	0.058	0.196	0.079	0.030
$\Delta Z_2$	0.002	0.123	<b>0.000</b>	0.316	0.175	0.082	0.060	0.058	1.000	0.436	0.637	0.023
$\Delta \omega_2$	0.079	0.037	<b>0.000</b>	0.156	0.371	0.058	0.052	0.196	0.436	1.000	0.077	0.103
$\Delta \phi_2$	0.062	0.017	<b>0.000</b>	0.141	0.099	0.041	0.092	0.079	0.637	0.077	1.000	0.124
$\Delta \kappa_2$	0.277	0.071	<b>0.000</b>	0.024	0.081	0.517	0.018	0.030	0.023	0.103	0.124	1.000

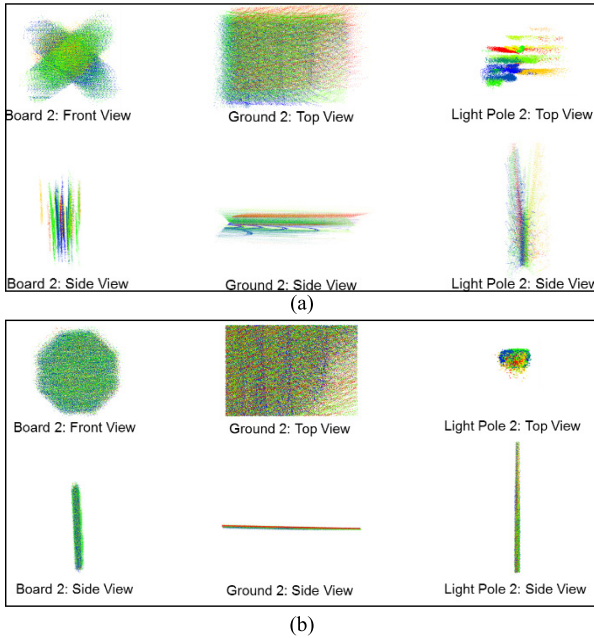


Fig. 10. Qualitative evaluation of some of the extracted boards, ground patches, and light poles. (a) Before calibration. (b) After calibration.

the estimated mounting parameters of the two sensors is listed in Table VII, which indicates that none of the parameters are highly correlated, i.e., the setup of target primitives and the drive run configuration used in this experiment are optimal to remove any correlation between the estimated parameters. The average accuracy after calibration can be quantified by the square root of the *a posteriori* variance factor ( $\hat{\sigma}_o$ ), which is 1.42 cm in this case. This is better than the expected accuracy of around 3 cm according to the accuracies of the hardware involved. Furthermore, through the qualitative evaluation depicted in Fig. 10, one can observe a significant improvement of boards, ground patches, and light poles after calibration. The  $\hat{\sigma}_o$  value of the LSA procedure and the RMSE of normal distance of points from best-fitting

TABLE VIII  
HDL-32E + VLP-16 MULTISENSOR CALIBRATION: *a Posteriori* VARIANCE FACTOR ( $\hat{\sigma}_o$ ) AND RMSE OF PLANE/LINE FITTING

	Number of Points	Before Calibration	Calibration Iteration 1	Calibration Iteration 2	Calibration Iteration 3
$\hat{\sigma}_o$ (m)			0.0149	0.0143	0.0142
Board 0 (m)	81,170	0.141	0.018	0.018	0.018
Board 1 (m)	75,182	0.124	0.019	0.019	0.019
Board 2 (m)	94,871	0.149	0.015	0.015	0.015
Board 3 (m)	72,303	0.111	0.018	0.018	0.018
Board 4 (m)	69,328	0.131	0.014	0.014	0.014
Ground 0 (m)	639,935	0.162	0.022	0.020	0.019
Ground 1 (m)	312,226	0.141	0.019	0.018	0.018
Ground 2 (m)	170,082	0.199	0.022	0.017	0.017
Wall 0 (m)	1,066,615	0.246	0.020	0.020	0.020
Pole 0 (m)	13,210	0.138	0.019	0.018	0.018
Pole 1 (m)	33,972	0.156	0.020	0.019	0.019
Pole 2 (m)	9,179	0.169	0.021	0.020	0.020

plane/line for extracted features after every iteration are listed in Table VIII.

## V. CONCLUSION

In this paper, we conducted a thorough bias impact analysis for terrestrial mobile mapping systems consisting of a spinning multibeam laser scanner, and validated the analytically driven conclusions by evaluating the results from an experimental setup. Based on this analysis, an optimal target primitive setup and drive run configuration is devised for calibrating a multisensor LiDAR system. Finally, an iterative calibration

strategy is proposed for deriving the mounting parameters of multiple sensors simultaneously. With the adopted modified weight matrix, the calibration procedure can utilize different types of conjugate features (i.e., planar, linear/cylindrical) at the same time. The proposed iterative calibration method is capable of deriving accurate mounting parameters, even if the initial estimates are considerably inaccurate. The multiunit LiDAR system calibration can reach an accuracy of 1–2 cm, which is better than the expected accuracy of around 3 cm, keeping in mind the accuracies of the hardware involved. This indicates that the proposed calibration strategy is efficient and accurate. Future work will focus on combining the mounting parameters (i.e., extrinsic parameters) and sensor parameters (i.e., intrinsic parameters) to obtain a comprehensive calibration leading to even more accurate point clouds. Also, the proposed calibration procedure would be evaluated on its performance to calibrate airborne laser scanning systems. This 3-D point-positioning-based approach for calibration can also be extended to GNSS/INS-assisted systems comprising of several cameras and laser scanners simultaneously to integrate the point clouds obtained from imagery and LiDAR data together.

#### ACKNOWLEDGMENT

The contents of this paper reflect the views of the authors, who are responsible for the facts and the accuracy of the data presented herein, and do not necessarily reflect the official views or policies of the sponsoring organizations.

#### REFERENCES

- [1] H. Lin *et al.*, “Semantic decomposition and reconstruction of residential scenes from LiDAR data,” *ACM Trans. Graph. TOG*, vol. 32, no. 4, 2013, Art. no. 66.
- [2] K. Williams, M. J. Olsen, G. V. Roe, and C. Glennie, “Synthesis of transportation applications of mobile LiDAR,” *Remote Sens.*, vol. 5, no. 9, pp. 4652–4692, 2013.
- [3] U. Weiss and P. Biber, “Plant detection and mapping for agricultural robots using a 3D LiDAR sensor,” *Robot. Auto. Syst.*, vol. 59, no. 5, pp. 265–273, 2011.
- [4] I. Puente, H. González-Jorge, J. Martínez-Sánchez, and P. Arias, “Review of mobile mapping and surveying technologies,” *Measurement*, vol. 46, no. 7, pp. 2127–2145, 2013.
- [5] A. F. Habib, A. P. Kersting, A. Shaker, and W.-Y. Yan, “Geometric calibration and radiometric correction of LiDAR data and their impact on the quality of derived products,” *Sensors*, vol. 11, no. 9, pp. 9069–9097, 2011.
- [6] B. Schwarz, “LiDAR: Mapping the world in 3D,” *Nature Photon.*, vol. 4, no. 7, p. 429, 2010.
- [7] J. Choi, “Hybrid map-based SLAM using a Velodyne laser scanner,” in *Proc. IEEE 17th Int. Conf. Intell. Transp. Syst. (ITSC)*, Oct. 2014, pp. 3082–3087.
- [8] B. Vallet, W. Xiao, and M. Brédif, “Extracting mobile objects in images using a Velodyne LiDAR point cloud,” *ISPRS Ann. Photogramm. Remote Sens. Spatial Inf. Sci.*, vol. 2, no. 3, pp. 247–253, 2015.
- [9] G. Atanacio-Jiménez *et al.*, “LiDAR Velodyne HDL-64E calibration using pattern planes,” *Int. J. Adv. Robot. Syst.*, vol. 8, no. 5, p. 59, 2011.
- [10] C. Glennie *et al.*, “Compact multipurpose mobile laser scanning system—Initial tests and results,” *Remote Sens.*, vol. 5, no. 2, pp. 521–538, 2013.
- [11] J. Underwood, A. Hill, and S. Scheding, “Calibration of range sensor pose on mobile platforms,” in *Proc. IEEE/RSJ Int. Conf. Intell. Robots Syst. (IROS)*, Oct./Nov. 2007, pp. 3866–3871.
- [12] N. Muhammad and S. Lacroix, “Calibration of a rotating multi-beam lidar,” in *Proc. IEEE/RSJ Int. Conf. Intell. Robots Syst. (IROS)*, Oct. 2010, pp. 5648–5653.
- [13] M. He, H. Zhao, F. Davoine, J. Cui, and H. Zha, “Pairwise LiDAR calibration using multi-type 3D geometric features in natural scene,” in *Proc. IEEE/RSJ Int. Conf. Intell. Robots Syst. (IROS)*, Nov. 2013, pp. 1828–1835.
- [14] T. O. Chan, D. D. Lichti, and D. Belton, “Temporal analysis and automatic calibration of the Velodyne HDL-32E LiDAR system,” *ISPRS Ann. Photogramm. Remote Sens. Spatial Inf. Sci.*, vol. 2, pp. 61–66, Oct. 2013.
- [15] C. L. Glennie, A. Kusari, and A. Facchini, “Calibration and stability analysis of the VLP-16 laser scanner,” *Int. Arch. Photogramm. Remote Sens. Spat. Inf. Sci.*, vol. 40, p. 55–60, Feb. 2016.
- [16] A. Habib, A. P. Kersting, K. I. Bang, and D.-C. Lee, “Alternative methodologies for the internal quality control of parallel LiDAR strips,” *IEEE Trans. Geosci. Remote Sens.*, vol. 48, no. 1, pp. 221–236, Jan. 2010.
- [17] E. Renaudin, A. Habib, and A. P. Kersting, “Featured-based registration of terrestrial laser scans with minimum overlap using photogrammetric data,” *ETRI J.*, vol. 33, no. 4, pp. 517–527, 2011.
- [18] Velodyne (a). (2016). *Velodyne HDL-32E User Manual*. Accessed: Feb. 20, 2017. [Online]. Available: [http://velodynelidar.com/docs/manuals/63-9113%20REV%20K%20MANUAL,USER'S,HDL-32E\\_Outlined.pdf](http://velodynelidar.com/docs/manuals/63-9113%20REV%20K%20MANUAL,USER'S,HDL-32E_Outlined.pdf)
- [19] Velodyne (b). (2016). *Velodyne VLP-16 User Manual*. Accessed: Feb. 20, 2017. [Online]. Available: <http://velodynelidar.com/docs/manuals/63-9243%20Rev%20B%20User%20Manual%20and%20Programming%20Guide,VLP-16.pdf>
- [20] Novatel. (2014). *Novatel SPAN-CPT User's Manual*. Accessed: Feb. 20, 2017. [Online]. Available: <http://www.novatel.com/assets/Documents/Manuals/om-20000122.pdf>
- [21] W. E. Wentworth, “Rigorous least squares adjustment: Application to some non-linear equations, I,” *J. Chem. Educ.*, vol. 42, no. 2, p. 96, 1965.



**Radhika Ravi** was born in India. She received the B.Tech. degree in civil engineering and the B.Tech. degree in electrical engineering from IIT Kanpur, Kanpur, India, in 2016. She is currently pursuing the M.S. degree in civil engineering (geomatics) with the Lyles School of Civil Engineering, Purdue University, West Lafayette, IN, USA.

Her research interests include 3-D point cloud reconstruction from LiDAR and photogrammetric data, intrinsic and extrinsic calibration of mobile LiDAR systems, and calibration of LiDAR systems integrated with several cameras.



**Yun-Jou Lin** was born in Taiwan. She received the B.S. and M.S. degrees in civil engineering from Nation Central University, Taoyuan City, Taiwan. She is currently pursuing the Ph.D. degree in geomatics with the Lyles School of Civil Engineering, Purdue University, West Lafayette, IN, USA.

Her research interests include point clouds processing (i.e., segmentation, reconstruction, and feature extraction) from mobile mapping LiDAR system, terrestrial LiDAR systems, and image-based point cloud.



**Magdy Elbahnaawy** received the B.Sc. and M.Sc. degrees in electrical engineering from the Military Technical College, Cairo, Egypt, in 2004 and 2012, respectively. He is currently pursuing the Ph.D. degree in interdisciplinary program geo-electrical which combines electrical and geomatics fields with the Lyles School of Civil Engineering, Purdue University, West Lafayette, IN, USA.

His research interests include multisensor integration for both terrestrial and aerial mapping systems, system calibration of LiDAR/imagery mapping systems, UAV-based 3-D mapping, and trajectory estimation in GNSS-denied areas using photogrammetric information.



**Tamer Shamseldin** received the B.S. and M.S. degrees in electrical engineering from the Military Technical College, Cairo, Egypt, in 2004 and 2012, respectively. He is currently pursuing the Ph.D. degree in interdisciplinary program geo-electrical between geomatics with the Lyles School of Civil Engineering and Electrical and Computer Engineering, Purdue University, West Lafayette, IN, USA.

His research interests include the development of system architecture for LiDAR-based UAV and terrestrial mapping systems, single and multi-LiDAR system calibration, and SLAM-assisted coverage path planning for indoor LiDAR mapping system.



**Ayman Habib** received the M.Sc. and Ph.D. degrees in photogrammetry from The Ohio State University, Columbus, OH, USA, in 1993 and 1994, respectively.

He is currently a Professor in geomatics with the Lyles School of Civil Engineering, Purdue University, West Lafayette, IN, USA.

His research interests include the fields of terrestrial and aerial mobile mapping systems, modeling the perspective geometry of nontraditional imaging scanners, automatic matching and change detection, automatic calibration and stability analysis of low-cost digital cameras, utilizing low-cost imaging systems for infrastructure monitoring and biomedical applications, incorporating analytical and free-form linear features in various photogrammetric orientation procedures, object recognition in imagery, UAV-based 3-D mapping, and integrating photogrammetric data with other sensors/data sets, such as GPS/INS, GIS databases, multispectral sensors, and LiDAR.